Crystallization and mechanical properties of a barium titanosilicate glass

Pierre Mezeix, T. To, Patrick Houizot, Fabrice Celarie, Tanguy Rouxel

Crystallization and mechanical properties of a barium titanosilicate glass

Pierre Mezeix [1], Theany To[1,*], Patrick Houizot[1], Fabrice Célarié[1], Tanguy Rouxel[1,2]

[1] *Mechanics and Glass department, Institute of Physics of Rennes, UMR 6251 UR1-CNRS, University of Rennes 1, Campus de Beaulieu, 35042 Rennes Cedex, France*

[2] *Institut Université de France (IUF)*

[*] Corresponding author. E-mail: theany.to@univ-rennes.fr; theany.to@gmail.com

Abstract

Glasses and glass-ceramics from the BaO-TiO_2-SiO_2 systems have potential applications in piezoelectric and photonic devices. However, more studies on their crystallization and mechanical properties are needed to put the materials into service. In this work, seven grades of glasses with $30BaO$-$xTiO_2$-$(70-x)SiO_2$ (mol%) were prepared. The crystallization behavior and mechanical properties were investigated. The $30BaO$-$20TiO_2$-$50SiO_2$ glass composition, possessing a glass transition temperature of 759 °C and a crystallization onset temperature of 877 °C, shows a prominent surface-nanocrystallization. Heat-treatments at 800 °C for different durations result in various depths for the crystalline phase layer. Depths of about 1 µm and 200 µm were obtained by heat-treatments for 3 h and 70 h, respectively. The nucleation rate is found to be around 10^{16} to 10^{18} m^{-3} s^{-1}, which is comparable to that of the fresnoite stoichiometric composition ($Ba_2TiSi_2O_8$). The hardness and Young's modulus of the crystalline layer are about 80% and 45% higher than those of the parent glass. The fracture behavior of this layer is highly anisotropic, as a result of the crystallization texture.

***Keywords*:** Glass, Glass-ceramic, Fresnoite, Indentation, Three-point bending

1

1. Introduction

Glass-ceramics, based on $BaO\text{-}TiO_2\text{-}SiO_2$ chemical system, have been extensively studied because of the good dielectric and nonlinear optical properties of the fresnoite crystal ($40BaO\text{-}20TiO_2\text{-}40SiO_2$) [1–10]. Most studies are interested in the nucleation and/or crystallization of the fresnoite in the glass system. For instance, Cabral et al. [5] showed that the crystal nucleation rate in the fresnoite glass system is about 10^{17} m^{-3} s^{-1}, comparable to that of the metallic glasses leading to nanostructure glass-ceramics. Enomoto et al. [7] were able to fabricate transparent glass-ceramic fibers containing fresnoite nanocrystals, exhibiting the second harmonic generation. Moreover, the patterning of the crystals at the surface of a fresnoite glass by laser irradiations was proposed as a new way of controlling the crystallization process [9, 10]. However, there is a lack of knowledge in the mechanical and especially cracking properties of these glass-ceramics. There are still not many studies on their mechanical properties [11–13]. Mechanical properties such as hardness (H) and Young's modulus (E) of the fresnoite glass-ceramics were studied, and 20% and 25% increases of H and E were obtained after 55% of the glass was crystallized [8]. Ghardi et al. [11] reported a study by means of molecular dynamics simulations that the elastic modulus of the fresnoite-type glasses increases with increasing the amount of TiO_2. Another study on the $30BaO\text{-}15TiO_2\text{-}55SiO_2$ system shows that the elastic moduli deceases with increasing the replacemant of SiO_2 by GeO_2 [13]. Sun et al. [12] reported that increasing the duration time of heat-treatment can increase the fracture toughness and hardness (but not the elastic moduli) of the glass-ceramics containing the fresnoite crystals. The fresnoite-type glass-ceramics were mostly reported to have the surface crystallization along the c-axis [14, 15], which might affect the characteristics measured based on the surface condition such as hardness and crack initiation resistance. As such, it is needed to be able to product large batches of the mother glasses to test the difference between the surface and the bulk properties of the fresnoite glass-ceramics.

This study focuses on $30BaO\text{-}x TiO_2\text{-}(70\text{-}x)SiO_2$ glasses (x varies from 0 to 30 mol%, and we note $x30$ stands for the studied glass with 30 mol% of TiO_2). Unlike the fresnoite compositions, $30BaO\text{-}x TiO_2\text{-}(70\text{-}x)SiO_2$ glasses are easy for glass-forming, allowing for relatively large batches of the bulk glasses to be obtained (in cm^3 dimension) [16], and thus further allowing for mechanical testing. In our previous study, we studied the elasticity and viscosity of these $30BaO\text{-}x TiO_2\text{-}(70\text{-}x)SiO_2$ glasses [17], while in this recent study, we focus on

2

their crystallization and mechanical properties. It was demonstrated, by means of X-ray diffraction (XRD) and differential scanning calorimetry (DSC) analysis, that $30BaO\text{-}20TiO_2\text{-}50SiO_2$ glass is prone to nanocrystallization, as will be further discussed. The crystallization kinetics and crystal orientation of this glass were determined by means of optical microscopy, scanning electron microscopy, and Raman spectroscopy. Vickers indentation and three-point bending tests were used to determine the hardness, elastic moduli, and fracture behavior of the $30BaO\text{-}20TiO_2\text{-}50SiO_2$ glass and glass-ceramics.

2. Experimental Procedures

The glass compositions examined in this study are listed in Table 1. The glass code *x*00 to *x*30 are named according to the amount of TiO_2 (in mol%), which substitutes for SiO_2. The glasses were prepared by a melt-quenching method using commercial powders from Sigma Aldrich and Pt-Rh crucible. All the experiment was performed in the ambient atmosphere (i.e., the room temperature of around 25 °C and relative humidity of around 45 %). In order to produce 50 g batches, we used adequate amounts of $BaCO_3$ (purity > 99%), TiO_2 (purity > 99%), and SiO_2 (purity > 99.9%) powders. The powder mixture was ball-milled for 10 min, placed in a Pt-Rh crucible, and heated in an electric furnace at 1500 to 1550 °C, depending on the viscosity of the melt, for 2 h. The melt was then quenched into a super-alloy (Inconel 600) mold pre-heated at T_g – 10 °C and further annealed at this T_g – 10 °C temperature for 5 h. Before cutting and polishing, the obtained glasses were reannealed at the measured T_g for 30 min to minimize the possible residual stress. The seven obtained glasses have less than 0.5 mol% difference between the nominal composition and the actual one as measured by energy-dispersive X-ray spectroscopy analysis (see measured composition in Table S1).

The glass transition (T_g), crystallization onset (T_x), crystallization peak (T_p), and melting (T_m) were measured by means of differential scanning calorimetry (DSC) at a heating rate of 10 °C min^{-1} under the N_2 flow of 10 mL min^{-1}, coupled with a thermogravimetric analysis (TGA) using an DTA/DSC SDT 2960 TA instrument. Each glass in the form of powder with a diameter of 100 to 200 μm was used in the DSC analysis. The glass powder was then heat-treated at its measured T_p for 6 h and cooled down slowly (~5 °C min^{-1}) to room temperature (~25 °C). The glass-ceramic powder was analyzed by X-ray diffraction, XRD, (using a PANalytical X'pert diffractometer) to determine the crystallization. A Bragg-Brentano D8 Advance diffractometry equipped with a rapid detector (LynxEye) and a heater (Paar HTK 1200) was used to determine

3

the temperature on the crystallization onset. Next, we chose a glass grade (depending on the information from the results of the DSC and XRD study) for deep study by in-situ X-ray diffraction at elevated temperature. The chosen glass powder was heated at a rate of 2 °C min^{-1} from room temperature to 900 °C. Before each acquisition temperature, we stabilized the temperature for around 5 min before recording the spectrum. The acquisition of one spectrum is around 4 min. Scanning electron microscopy (SEM) observations were conducted for some glass-ceramics.

Vickers indentation at room temperature was used to determine indentation cracks, hardness (H), and reduced modulus (E_r), and of the glass and glass-ceramic. A set of indentation loads (0.02, 0.1, 0.2, 0.3, 0.4, 0.5, 0.7, 1 and 3 N) were used in these indentation studies. The indentation cracks were studied by a microindenter (Fisherscope H100) for the loads of 0.02, 0.1, 0.5, and 1 N, and by another microindenter (Matsuzawa VMT-7S) for the loads of 3N. To observe the indentation cracks, the SEM was used for the load smaller than 1 N, and an optical microscope (Olympus BX60) was used for the load from 1 N. Hardness and reduced modulus of the *x*20 glass, glass-ceramic heat-treated for 8 h at 800 °C, were determined by the Fisherscope microindenter using the loads of 0.1, 0.2, 0.3, 0.4, 0.7, and 1 N. We note that the indentation to measure H and E_r of the glass-ceramic were performed on the heat-treated surface, i.e., on the ab-plan (plan paralleled to the crystal orientation). H and E_r were then calculated from Eq (1) and (2) [18–21], respectively.

$$H = \frac{P_i}{A_c}, \qquad (1)$$

$$E_r = \frac{\sqrt{\pi}}{2}\frac{S_{unl}}{\beta\sqrt{A_c}}, \qquad (2)$$

where P_i is the maximum indentation load, A_c is the indent projected contact area, S_{unl} is the slope of the initial unloading curve, β is the indenter geometric factor (β = 1.012 in case of a Vickers indenter). To find S_{unl}, first, as mentioned in the Oliver-Pharr method [20], the data taken from the upper portion of the unloading curve are fitted by a power-law as in Eq. (3),

$$P_i = n\,(h - h_f)^m, \qquad (3)$$

4

where h and h_f are the elastic displacement and the residual depth, respectively, while n and m are empirical constants determined after the unloading data fitting. Then, h_f can be calculated from Eq. (3) by taking $P_i = P_{i\_max}$ and $h = h_{max}$. S_{unl} is calculated from Eq. (4) below,

$$S_{unl} = \frac{dP_i}{dh} = m\, n\, (h_{max} - h_f)^{m-1}. \qquad (4)$$

For the projected contact area A_c, we employ the equation of the area function as $A_c = 24.5h_c^2 + 6300h_c + 3150\, h_c^{0.5} + 3150\, h_c^{0.25} + 3150h_c^{0.125} + 3150h_c^{0.0625} + 3150h_c^{0.03125} + 3150h_c^{0.015625}$, where h_c is in nm and $h_c = h_{max} - 0.75P_{max}\,(S_{unl})^{-1}$ [21]. To get the constant coefficients in this area function, the compliance of the Fischerscope H100 and the bluntness of the Fischer Vickers indenter tip were used in the fitting process.

The elastic modulus was also measured by means of three-point bending method. For the three-point bending test, the specimen of a dimension of 25×3.9×0.97 mm^3 (L×B×W, where L, B, and W are the specimen length, breadth, and width (or height)) was loaded under a cross-head speed of 0.02 μm s^{-1} until reaching a load (P) of 2 N. To precisely measure the sample displacement, a laser interferometer displacement sensor (LK-G5000 series with LK-H008W head sensor, Keyence Corporation company of Japan) was used to measure the middle of the sample under three-point bending load [22].

3. Results and discussions

3.1. Synthesis

The glass composition diagram and a photo of the synthesized glass samples are shown in **Figure 1**. As indicated in the introduction, the 30BaO-$x$$TiO_2$-(70-$x$)$SiO_2$ glass compositions were chosen instead of ones including the fresnoite compositions because of the ease in producing large batches of glasses (in cm^3 diameter) [16], thus further allowing for mechanical testing. The substitution of TiO_2 for SiO_2 leads to the color changes, while glasses are homogenous, dense, transparent, and colorless for x00 and x05, then become yellowish for x10, x15, and x20, and finally brownish for x25 and x30.

3.2. Thermal properties of glasses and crystalline phase

The DSC curves of the different grades are shown in **Figure 2**, and the corresponding thermal properties are shown in **Table 1**. T_g increases with increasing the TiO_2 content, ranging from 705 °C for x00 to 762 °C for

5

*x*30. In all glasses, crystallization peaks were observed. For *x*30, there is a clear and rather sharp crystallization peak, suggesting the formation of a single crystalline phase. As shown in **Table 1**, T_x increases from 821 °C for *x*00 to 889 °C for *x*15 and decreases from *x*15 to 830 °C for *x*30. T_p and T_m show similar trends with the maxima of 932 and 1224 °C and the minima of 841 and 1205 °C, respectively. The differences between T_x and T_g (i.e., $T_x - T_g$) initially increase from *x*00 (116 °C) to *x*05 (141 °C) and then decrease to *x*30 (68 °C). As noted in Section 2, $T_x - T_g$ is a measure of thermal stability against crystallization. The glasses, with $x > 20$ mol%, exhibit a relatively small $T_x - T_g$ interval in comparison to the other glasses, showing easiness in crystallization. This easiness makes the control of the crystallization difficult for the *x*25 and *x*30 grades. Consequently, surface crystals can hardly be avoided during the cooling stage from the melt. Compositions with $x < 20$ mol% are more stable according to the high $T_x - T_g$. However, these glasses exhibit broad crystallization peaks, suggesting the formation of two or more crystalline phases, as seen in the *x*00. While having $T_x - T_g$ larger than that of *x*00, *x*20 has a more apparent crystallization peak compared to all compositions with $x < 20$ mol%. This is a favorable situation for controllable crystallization. Moreover, *x*20 ($Ba_{1.5}TiSi_{2.5}O_{8.5}$) has a relatively close composition compared to that of the fresnoite ($Ba_2TiSi_2O_8$).

The XRD patterns for the studied samples after heat-treatment at T_p for 6 h are presented in **Figure 3**. The peaks associated with the crystallized phases are in agreement with $Ba_2TiSi_2O_8$ (ICDD: 00-022-0513) or $BaSi_2O_5$ (ICDD: 00-004-0382) compounds depending on the TiO_2 content in the glasses. The compositions with a small amount of TiO_2 (i.e., *x*00 and *x*05) have a similar structure to that of $BaSi_2O_5$. As seen in **Figure 3**, these compositions exhibit a sharp peak at $2\theta \sim 22.2°$ and several peaks at 2θ between 38.3 and 41.5°. In the *x*05, we observe the presence of a small peak at 23.3°, consistent with the $Ba_2TiSi_2O_8$ phase. This indicates the influence of the addition of TiO_2. For the *x*10, the peaks at 22.2° and between 38.3 and 41.5° become smaller, the peak at 23.3° remains the same, the peak at 28.7° becomes (totally) 29° and there exists a peak at 33.2°, suggesting the disappearance of the $BaSi_2O_5$ crystals and the appearance of $Ba_2TiSi_2O_8$ ones. In other word, the XRD of the x10 shows the existence of both $BaSi_2O_5$ and $Ba_2TiSi_2O_8$ crystals as indicated in Figure S0 in the SI, and seen in the broadness of the DSC curves (Figure 2). From Figure S0a and S0b, we see that *x*10 has the peaks at 22.2° (with the intensity of half of the largest peak at 29° of this *x*10 glass-ceramic) and 22.2° similar to those of $BaSi_2O_5$, together with the peaks at 29° (vanishing of the peak at 28.7°), at 33.2° and 34.4° similar to those of the fresnoite crystal. For *x*15-*x*30, they have similar peak positions and intensities in the

6

XRD pattern. The peaks of these compositions are like those of the $Ba_2TiSi_2O_8$. We note that the existence of both $BaSi_2O_5$ and $Ba_2TiSi_2O_8$ crystals is not observed in the *x*15 as in *x*10 and as discussed in the DSC section. For *x*15-*x*30, the *x*20 composition exhibits peaks at 2θ = 17 and 34.4°, which are more intense than for the other grades. These peaks correspond to the (001) and (002) planes, respectively [23]. This confirms that the *x*20 is a prominent composition for crystallization also in the sense of textural material designs.

3.3. Crystallization of *x*20

The *x*20 glass was observed by in-situ XRD during heating from room temperature (25 °C) to 900 °C with a rate of 2 °C min^{-1}. **Figure 4** shows the XRD patterns for the *x*20 sample from 795 to 820 °C. From room temperature to 795 °C, there is no peak on the XRD patterns, indicating that the sample remains amorphous. At 800 °C, there exist two crystalline peaks at 2θ ~27 and 29°. At 805 °C, the two crystalline peaks grow larger and more tiny peaks can be seen in the spectrum. However, the temperature that the peaks are relatively large, stable and close to those of the fresnoite starts from the temperature of 810 °C (**Figure 4**). Hence, the temperature between 795 to 800 °C is the starting point of the fresnoite crystallization.

It was found from SEM analyses for the broken *x*20 beam sample that crystals are formed only at the surface but not in the interior of the glass. This only-surface crystallization is also verified by the result from micro-Raman experiment as seen in Figure S2 in the Supporting Information. **Figure 5a** shows the way that the SEM observation was performed. As seen in **Figure 5b**, the broken surface (the interior of the sample) does not show any crystallization, although the heat-treatment above T_g (= 759 °C) might affect the glass structure (**Figure 5c**), while the treated surfaces show intensive crystallization (**Figure 5d**). The size of crystals is ~200 nm, as shown in **Figure 5d**. The sizes of the crystals and the depth of the crystalline phases depend on the duration of the heat-treatment (see Section 3.4). The obtained glass-ceramic is found to have better transparency and less color than the mother *x*20 glass under the naked eye observation (see Figure S1 in the Supporting Information).

3.4. Kinetics of crystallization of *x*20

Figure 6 shows the SEM images of the *x*20 glass-ceramics heat-treated at 800 °C for durations of 1 h to 16 h as marked on the images as 1H to 16H, respectively. It can be seen clearly that the size of the crystals increases with increasing the heat-treatment duration time. Within 2 h, the crystal diameter increases to ~ 0.2 μm, while

7

within 16 h, the diameter increases to ~ 0.9 μm. From this observation, we can calculate the crystal diameter (D in μm) as a function of time (t in h) as $D = 0.234t^{0.5}$ with a regressive coefficient R^2 of 0.9598 (**Figure 7**). The time exponent (0.5) suggests that crystallization is controlled by diffusion [24]. Nevertheless, there might be some incubation time before growth starts, for about 1 h, as a better fit is obtained with $D = \alpha(t-1)^{0.5}$ (α = 0.252 in **Figure 7**).

The depth (z) of the crystalline phase is also related to the heat-treatment time, as shown in **Figure 8**. For $t \leq$ 1 h, z is smaller than 1 μm. For 4 h, the z increases to 3 μm, and for 75 h, the z increases to 220 μm. We can then calculate the evolution of the crystalline depth (z in μm) as a function of heat-treatment time (t in h) to be $P = 0.2899t^{1.6296}$ (**Figure 9**). With z and D, we can then calculate the crystal volume (V) as a function of heat-treatment time. V of a crystallite is equal to $(z/D)\ \pi\ (D^3/6)$, $z\ \pi\ (D^2/4)$, or $(z/3)\ \pi\ (D^2/4)$ in the cases of spherical, cylindric, or conical forms, respectively [25]. From the glass (ρ_g), glass-ceramic (ρ_{gc}), and the crystal (ρ_c) densities, we can then calculate the volume fraction of crystals (f) to be $f = (\rho_{gc} - \rho_g)\ (\rho_c - \rho_g)^{-1}$. **Figure 10** shows the evolution of f (in %) as a function of t (in h). The f can be estimated as $f = 0.0103\ t^{0.6096}$. With f and V, the nucleation rate (I) can be calculated as $I = f\ V^{-1}\ t^{-1}$ [26].

The nucleation rate as a function of heat-treatment time ($I = f\ V^{-1}\ t^{-1}$) is shown in **Figure 11**. In the case of spherical crystals, the crystallization rate starts increasing after 3 h of heat-treatment. This shows that the crystal shape is likely to be conic or cylinder. From **Figure 11**, the nucleation rate of *x*20 heat-treated at 800 °C is around 10^{16} to 10^{18} m^{-3} s^{-1}; the rate decreases with increasing the treatment time. This I value agrees well with the nucleation rate of a similar glass [5].

3.5. Hardness, elasticity, and cracking behavior of *x*20 glass and glass-ceramic

Figure 12 shows the load-displacement and unloaded-displacement curves of all the applied loads for the *x*20 glass and the glass-ceramic (*x*20 heat treated for 8 h at 800 °C). This glass-ceramic has a crystalline layer thickness of around 20 μm, which is expected to be thick enough to get the real crystalline layer indentation properties (at low load) and thin enough to see the substrate influence (at large load). It can be seen that for the same maximum load, all the maximum displacement and the residual depth for glass are greater than those for its glass-ceramic counterpart, while the slope of the unloading curve for those materials is similar at the load smaller than 400 mN and different at the load greater than (and equals to) 400 mN (see Figure S3 in

8

Supporting Information). From the indentation load of 400 mN, the slope of the unloading curve of the glass-ceramic is smaller than that of the glass counterpart (Figure S3). This difference may indicate the influence of the glass substrate on the elasticity of the crystalline layer (see next two paragraphs for detailed discussion).

Figure 13 shows the hardness and reduced modulus of the glass and the glass-ceramic (*x*20 heat treated for 8 h at 800 °C, noted as GC_8h) calculated from Eqs. (1-4) and plotted as a function of the indentation depth. From Figure 13a, we see that the hardness of glass (H ~ 6 GPa) is smaller than that of the glass-ceramic (H ~ 12 GPa) for all the tested indentation depth. The hardness seems to be constant and independent of the indentation depth, even for the case of the glass-ceramic with the crystalline thickness, z, of about 20 μm. The constant hardness of a homogenized material (in our case, the glass) is expected when using the Oliver Pharr method through the area function that concerns the stiffness of the machine and the bluntness of the indenter tip [21]. As such, the indentation size effect is not observed in the measured hardness using this method (Figure 13a). For the case of the thin film on the substrate (in our case, the glass-ceramic with z ~ 20 μm), it is recommended to measure the hardness at the depth lower than 10 % of the film thickness (i.e., at $0.1z$ = 2 μm) when the film is harder than the substrate because the substrate yields at indentation depth less than the film thickness [27]. In our case, even though the crystalline layer (the film) is twice harder than the glass substrate (Figure 13a), the hardness seems to be constant or slightly (in the error range) decrease if the H at h ~ 0.6 μm is not considered. The difference of H as a function of indentation depth is not significant maybe because the maximum depth of the measured H in this study is not more than 15% z. In fact, the measurement of the indentation hardness is less affected by the substrate compared to the indentation modulus because the elastic filed under the indenter is a long-range field extending into the substrate [27, 28].

A plot of the reduced modulus of the *x*20 glass and GC_8h as a function of indentation depth is shown in Figure 13b. The reduced modulus of the glass is around 80 GPa and independent of the indentation depth. In contrast, the reduced modulus of the GC_8h is about 120 GPa at the h less than 1.2 μm, 100 GPa at h = 1.5 μm, and 80 GPa at h more than 2 μm. As mentioned earlier, it is expected to see that the reduced modulus decreases with increasing the indentation depth because of the long-range elastic field extending into the substrate. The decrease of E_r of GC_8h to that of the glass at h > 2 μm (P_i > 500 mN) maybe because of (i) the force of 500 mN (h > 10% z) is large enough to transform all the elastic energy from the indenter to the substrate

9

since the indentation in c-axis direction and the layer is twice harder than the glass substrate, or (ii) there is a gradient of modulus in the c-axis direction as the crystalline layer may consist of small amount of glassy phase (Section 3.4).

To see the influence of maximum indentation loads on H and E_r, Joslin and Oliver [29] used the ratio of the load to the stiffness squared, $P_i\, S_{unl}^{-2}$, which can be measured directly from the experiment and independent of the h_c and A_c provided H and E_r do not vary with depth. $P\, S_{unl}^{-2}$ can be obtained from Eqs. (1) and (2) as,

$$\frac{P_i}{S_{unl}^2} = \frac{\pi}{(2\beta)^2}\,\frac{H}{E_r^2}. \qquad (5)$$

Figure 14 shows the $P_i\, S_{unl}^{-2}$ ratio as a function of indentation depth of the glass and the glass-ceramic. Similar to the trend of the slope of the unloading curves shown in Figure S3, the $P_i\, S_{unl}^{-2}$ ratios of the glass and the glass-ceramic start to differ from the load of around 400 mN (i.e., the indentation depth of around 1.5 μm for the glass-ceramic). In the case of glass, the ratio is constant as expected after Eq. (5) since the H and E_r of a homogenized material should also be constant (Figure 13). For the glass-ceramic, the ratio seems to be stable at the small indentation depth and start increasing from the indentation depth of 1.2 μm to 2 μm. The $P\, S_{unl}^{-2}$ ratio seems to be stable again when the indentation depth is higher than 2 μm, which is the 10 % of the thickness of the crystalline layer, z. Again, it is recommended to measure the hardness of the layer at the depth of less than $0.1t$ in the case of hard layer on a soft substrate. However, in the range of our measurement ($2.5\%\, z < h < 15\%\, z$), H seems to be constant and independent of h. Then, after Eq. (5), the $P\, S_{unl}^{-2}$ ratio depends solely on E_r. As a result, $P\, S_{unl}^{-2}$ and E_r have a reversed trend to each other (Figure 13b and 14). To minimize the effect of the substrate (glass) on the film (crystalline layer), we take E_r measured from the small indentation depth, where there is a plateau, which is 120 ± 2 GPa. The effective Young's modulus of the crystallized layer ($E_l' = E_l\,(1 - \nu_l^2)^{-1}$) can be calculated as,

$$\frac{1}{E_r} = \frac{(1-\nu_i^2)}{E_i} + \frac{(1-\nu_l^2)}{E_l}, \qquad (6)$$

where E_i and ν_i are Young's modulus and Poisson's ratio, respectively, of the indenter (for diamond indenter tip, E_i = 1140 GPa and ν_i = 0.07), and ν_l is the Poisson's ratio of the crystalline layer. We can then calculate E_l'

10

$= E_l (1 - \nu_l^2)^{-1} = 134 \pm 2$ GPa. Using the same Eq. (6), the effective Young's modulus of the glass is calculated to be $E_g^{'} = E_g (1 - \nu_g^2)^{-1} = 86 \pm 2$ GPa. Using the Poisson's ratio of the *x*20 glass measured from ultrasonic echography, $\nu_g = 0.280$ [17], $E_g = 79 \pm 2$ GPa, which is in good agreement with that from the literature (81 ± 1 GPa) [17]. It has been shown that the Poisson's ratio has a minor effect on the indentation result [30]; hence, we use the $\nu_l = 0.280$ to calculate the $E_l = 123 \pm 2$ GPa. This Young's modulus will be used to compare to that from the three-point bending method.

For the three-point bending experiment, we use an *x*20 glass and glass-ceramic (*x*20 heat-treated at 800 °C for 30 h) that has the crystalline layer thickness of, *z*, 80 ± 5 μm. The choice of a specimen with thicker crystalline layer than that of the indentation study is to see the influence of the crystalline layer stiffness because the calculated modulus in the three-point bending is sensitive to the specimen dimension and does to the layer. Figure 15 shows the load-deflection curve of the three-point bending test of the glass and the glass-ceramic with the same dimension. It can be seen that the slope of the glass-ceramic (orange line in Figure 15) is only slightly larger than that of the glass (blue line in Figure 15). This indicates that the glass-ceramic is only slightly stiffer than the glass. The Young's modulus (*E*) of the glass and the glass-ceramic were calculated from these load-deflection curves (Figure 15) as,

$$E = \frac{PS^3}{48\delta I}, \qquad (7)$$

where *P* is the applied load, δ is the specimen deflection, *S* is the span length of the three-point bending fixture, and *I* is the moment of inertia (for a rectangular shape, $I = BW^3/12$, where *B* is the specimen breadth and *W* is the height). To facilitate the discussion, we note indices "g" and "gc" to stand for "bulk glass" and "bulk glass-ceramic", respectively. Summary results for the following discussing are listed in Table S2. $P\,\delta^{-1}$ is determined as the slope of the load-deflection curve and found to be 0.2333 and 0.2001 N μm^{-1} for glass-ceramic and glass, respectively. Since the bulk glass and glass-ceramic specimens have the same dimension ($B = 3.9 \pm 0.002$ mm, $W = 0.97 \pm 0.002$ mm), then $I_g = I_{gc} = 0.2966$ mm^4. With *S* of 18 ± 0.002 mm, we calculate the Young's moduli of the glass and the glass-ceramic from Eqs. (7) and (8) to be 82 ± 2 and 95 ± 2 GPa, respectively. The glass ceramic in this study is composed of the glass substrate (indexed as "s") and the crystalline layer (indexed as "l") (see Table S2). The glass substrate should have the same Young's modulus

11

as that of the glass, which is $E_s = E_g = 82 \pm 2$ GPa. Since the glass substrate has smaller dimension ($B_s = B - 2z$ and $W_s = W - 2z$, where $z = 0.08 \pm 0.005$ mm) compared to the tested glass, I_g and $P_s\ \delta_s^{-1}$ slope are also relatively smaller. We calculate these two parameters from the dimension and Eq (7) or (8), respectively, to be $I_s = 0.1656$ mm^4 and $P_s\ \delta_s^{-1} = 0.1117$ N μm^{-1}. The moment of inertia of the crystalline layer, with the thickness $z = 0.08 \pm 0.005$ mm, could then be calculated as $I_l = I_{gc} - I_g = 0.1310$ mm^4. To calculate $P_l\ \delta_l^{-1}$ slope, we suppose that during loading the crystalline layer has the same deflection as those of the glass-ceramic and the glass substrate. To have $\delta_l = \delta_{gc} = \delta_s$, the force applied on the glass-ceramic should be decomposed into the force on the substrate and on the layer, which is $P_{gc} = P_s + P_l$ (or $P_l = P_{gc} - P_s$). In this case, $P_l\ \delta_l^{-1} = (P_{gc} - P_s)\ \delta_l^{-1} = P_{gc}\ \delta_{gc}^{-1} - P_s\ \delta_s^{-1} = 0.1216$ N μm^{-1}. Using Eq (7) or (8), the Young's modulus of the crystalline layer is calculated to be 113 ± 3 GPa. This Young's modulus value is a bit lower than that calculated from the indentation (123 ± 2 GPa). The explanation to this may be because the there is a gradient in elasticity in the c-axis of the crystalline direction since the indentation modulus is the surface measurement, and the bending modulus is the average measurement on the thickness *z*. We note that this increase in the Young's modulus of the glass-ceramic surface is around 40 % (by bending method) and 54 % (by indentation method) compared to the based *x*20 glass. This is similar to the increase of Young's modulus (by 56%) in the fresnoite glass-ceramic compared to its based glass ($40BaO\text{-}20TiO_2\text{-}40SiO_2$) [8].

The cracking behavior of the *x*20 glass and glass-ceramic (heat-treated for 75h at 800 °C) were studied by the Vickers indentation using a range of loads of 0.02, 0.1, 0.5, 1, and 3 N. Before the experiment, both glass and glass-ceramic were first re-annealed at the T_g of the glass for 30 min to remove the possible residual stresses on the material surface. The indentation was performed on a surface polished down to a 1 μm surface finish and the imprints are illustrated in **Figure 16a**. For the glass-ceramic in particular, the indentation was performed on the bc-plane as illustrated in **Figure 16b**. The indentation cracking behavior of the glass-ceramic is different from the one of the glass (**Figure 16a**). For the glass, the indentation of 0.02 N, does not produce any crack. Some corner cracks are seen after the load of 0.1 N, and 4 corner cracks are observed after the load of 0.5 N. For the crystalline layer, the cracks are only seen in the direction perpendicular to the c-axis for all the applied indentation load, although the crack length increases with increasing load. The indentations on different positions of the crystalline layer shows the same cracking behavior as seen in Figure S5 of the supporting information. This indicates that the crack initiation resistance of the crystalline layer is anisotropic,

12

and the crack initiation resistance in the crystalline direction (c-axis) is much greater than that in the direction perpendicular to the c-axis.

To explain this anisotropy in the crack resistance, we note that the fresnoite consists of a layer of Ba-O and a layer combined from the TiO_5 and Si_2O_7 groups, as seen in **Figure 17** [23]. It is noteworthy that the bond energy, as suggested by Sun. [31], of the Ba-O, Ti-O, and Si-O are 138, 305, and 444 kJ mol^{-1}, respectively. Apparently, it is easy to break the Ba-O bond than to break the combination of Ti-O and Si-O bonds. As seen in **Figure 17**, for a crack to grow on the c-axis, it needs to break all three bond types, while it needs to break only the Ba-O bonds on the b-axis. To compare the resistance to crack propagation between each possible path, we calculate theoretical fracture surface energy (γ^t) based on the ab-initial model as in Ref. [32] by assuming that there is no plasticity in the fracturing process. γ^t can be then predicted based on the experimental density, the molar mass, the bond strength, and the bond concentration along a fracture path or surface. Table 2 shows all γ^t of the glass and the glass-ceramics with different possible paths and directions. For the glass, we assume that during fracture, the crack propagates through one bond in each oxide unit, i.e., Ba-O, Ti-O, and Si-O bonds, in the BaO_y, TiO_y, and SiO_y units, respectively, where y is the number of oxygen atoms connected to the main atom in the glass structure. For the glass-ceramic layer, we assume that the crack propagates through path 1 (through b-axis), path 2 (through b-axis), or path 3 (through c-axis) as indicated in **Figure 17**. In path 1, the crack needs to travel through three bonds of Ba-O in a BaO_8 unit without breaking any other bonds of Ti-O or Si-O. For path 2, the crack needs to travel through one bond of the Ti-O in a TiO_5 unit and one bond of the Si-O in a SiO_4 unit without breaking any bond of Ba-O. For path 3, the crack needs to travel through the c-axis direction, i.e., it needs to break at least three bonds of Ba-O in a BaO_8 unit, at least one bond of the Ti-O in a TiO_5 unit, and at least one bond of the Si-O in a SiO_4 unit. We found that the energy needed for a crack to travel through path 1 or path 2, i.e., in the b-axis direction, is lower than that needed for a crack to travel through path 3 in the c-direction or through the bulk glass. We conclude that for the glass-ceramic layer, the crack travels through path 1, and it is even easier to fracture through path 1 than to fracture the bulk glass. This is in good agreement with the indentation fracture test, as shown in **Figure 16**. With an indentation load of 20 mN, there is no corner crack in the bulk glass, but there are already cracks in the b-axis direction in the glass-

13

ceramic layer. Moreover, there is no crack observed in the c-axis direction even when an indentation load as great as 3 N is applied.

4. Conclusion

In this paper, we have studied the crystallization behaviors and mechanical properties of glass grade chosen from the seven glasses in the 30BaO-xTiO$_2$-(70 – x)SiO$_2$ (mol%) system. Based on the DSC and XRD investigation, the 30BaO-20TiO$_2$-50SiO$_2$ (x20) grade, with T_g of 759 °C and T_x of 877 °C, showed a prominent surface crystallization with oriented crystals as those of the fresnoite. The in-situ XRD study on x20 grade shows that the onset temperature of crystallization is around 800 °C. At this temperature, the x20 grade was heat-treated at different duration time resulting in different crystalline layer. The 75 h heat-treated glass-ceramic has the crystalline layer of 220 μm, and is more transparent/colorless than that of the bulk glass. By calculating the nucleation rates of the x20 corresponding to the heat-treatment time with three different crystallite forms (i.e., sphere, cylinder, and cone), we see that the crystallite form is more likely to be cylinder and cone with a nucleation rate of around 10^{17} m^{-3} s^{-1}. Then, the mechanical properties of the glass-ceramic is studied by indentation and three-point bending experiments. The hardness calculated from indentation test at different depths is stable for both glass and glass-ceramic, and the hardness of the glass-ceramics is twice as large as the one of the glasses. Unlike the hardness, the indented reduced modulus of the glass-ceramic start to decrease from 120 GPa at the indentation depth of 5 % of the crystalline layer and is equals to that of the glass (80 GPa) when the depth reaches 10 % of the crystalline layer. This is due to the influence of the relatively hard and stiff layer (the crystalline layer) on the relatively soft and compliant substrate (the glass substrate). In contrast, the reduced modulus of the bulk glass does not vary with indentation depth indicating the homogeneity of the bulk glass. The elastic modulus of the crystalline layer calculated from the indentation at small load (the indentation depth of less than 5 % of the crystalline layer) has a good agreement with that calculated from the three-point bending test. The Vickers indentation study has also shown that the cracking behavior of the crystalline phase is anisotropic. Cracks tend to follow the easiest path, which is perpendicular to the c-axis. According to the fracture surface energy calculation, it proposes that the crack propagates through the line of the Ba-O bonds in the fresnoite crystallites, showing good agreement with the indentation crack experiment. The above result shows that x20 is a good candidate for producing c-axis oriented crystals on the

14

glass surface with heat-treatment, and this surface crystallization can be used to tune the mechanical properties of the glass in oriented direction.

Acknowledgments

We thank Nathalie Audebrand (UR1) for valuable discussion. This work was supported by the European Research Council through the ERC Advanced Grant 320506.

Author contributions

Pierre Mezeix - Conceptualization, Investigation, Methodology. Theany To – Conceptualization, Formal Analysis, Investigation, Writing – Original Draft, Writing – Review & Editing. Patrick Houizot – Investigation, Methodology. Fabrice Célarié - Investigation, Methodology. Tanguy Rouxel – Conceptualization, Methodology, Validation, Writing – Review & Editing.

Competing interests

The authors declare no competing financial interests.

Data and code availability: Not Applicable.

Supplementary information

SI1, Figure S1-3 are found in the supplementary information.

Ethical approval: Not Applicable.

References

1. Wisniewski W, Thieme K, Rüssel C (2018) Fresnoite glass-ceramics – A review. Prog Mater Sci 98:68–107. https://doi.org/10.1016/j.pmatsci.2018.05.002
2. Honma T, Maeda K, Nakane S, Shinozaki K (2022) Unique properties and potential of glass-ceramics. Journal of the Ceramic Society of Japan 130:545–551. https://doi.org/10.2109/jcersj2.22037

15

3. Jain H (2004) Transparent Ferroelectric Glass-Ceramics. Ferroelectrics 306:111–127. https://doi.org/10.1080/00150190490458446

4. Yamazawa T, Honma T, Suematsu H, Komatsu T (2009) Synthesis, ferroelectric and electrooptic properties of transparent crystallized glasses with $Sr_xBa_{1-x}Nb_2O_6$ nanocrystals. Journal of the American Ceramic Society 92:2924–2930. https://doi.org/10.1111/j.1551-2916.2009.03348.x

5. Cabral AA, Fokin VM, Zanotto ED, Chinaglia CR (2003) Nanocrystallization of fresnoite glass. I. Nucleation and growth kinetics. J Non Cryst Solids 330:174–186. https://doi.org/10.1016/j.jnoncrysol.2003.08.046

6. Halliyal A, Safari A, Bhalla AS, et al (1984) Grain-oriented glass-ceramics for piezoelectric devices. Journal of the American Ceramic Society 67:331–335. https://doi.org/10.1111/j.1151-2916.1984.tb19532.x

7. Enomoto I, Benino Y, Fujiwara T, Komatsu T (2007) Chemically etched sharpened tip of transparent crystallized glass fibers with nonlinear optical $Ba_2TiSi_2O_8$ nanocrystals. Journal of the Ceramic Society of Japan 115:374–378. https://doi.org/10.2109/jcersj.115.374

8. Shinozaki K, Honma T, Komatsu T (2011) Elastic properties and Vickers hardness of optically transparent glass–ceramics with fresnoite $Ba_2TiSi_2O_8$ nanocrystals. Mater Res Bull 46:922–928. https://doi.org/10.1016/j.materresbull.2011.02.031

9. Honma T, Komatsu T, Benino Y (2008) Patterning of c-axis-oriented $Ba_2TiX_2O_8$ (X = Si, Ge) crystal lines in glass by laser irradiation and their second-order optical nonlinearities. J Mater Res 23:885–888. https://doi.org/10.1557/JMR.2008.0135

10. Zhu B, Dai Y, Ma H, et al (2008) Direct writing Eu^{+3}-doped $Ba_2TiSi_2O_8$ crystalline pattern by femtosecond laser irradiation. J Alloys Compd 460:590–593. https://doi.org/10.1016/j.jallcom.2007.06.034

11. Ghardi EM, Atila A, Badawi M, et al (2019) Computational insights into the structure of barium titanosilicate glasses. Journal of the American Ceramic Society 102:6626–6639. https://doi.org/10.1111/jace.16536

12. Sun D, Zhang Q, Liu P, et al (2023) Balancing fracture toughness and transparency in barium titanosilicate glass-ceramics. Ceram Int 49:17479–17487. https://doi.org/10.1016/j.ceramint.2023.02.115

13. Masai H, Fujii Y, Kitamura N, Yamawaki M (2022) Relationship between the elastic properties and structure of $BaO\text{-}TiO_2\text{-}GeO_2\text{-}SiO_2$ glasses. J Non Cryst Solids 576:121248. https://doi.org/10.1016/j.jnoncrysol.2021.121248

14. Masai H, Okada G, Kawaguchi N, Yanagida T (2018) Photoluminescence and X-ray-induced scintillation of $BaO\text{-}TiO_2\text{-}SiO_2$ glasses and the glass-ceramics. J Non Cryst Solids 501:131–135. https://doi.org/10.1016/j.jnoncrysol.2017.11.026

16

15. Lee HK, Lee YS, Bhalla AS, Kang WH (2006) Preparation and properties of transparent glass-ceramics in xK$_2$O-(33.3 − x)BaO-16.7TiO$_2$-50SiO$_2$ Glasses. Ferroelectrics 330:9–18. https://doi.org/10.1080/00150190600605361

16. Cleek GW, Babcock CL (1973) Properties of glasses in some ternary systems containing BaO and SiO$_2$. NBS report 135:1–39

17. Mezeix P, Célarié F, Houizot P, et al (2016) Elasticity and viscosity of BaO-TiO$_2$-SiO$_2$ glasses in the 0.9 to 1.2T_g temperature interval. J Non Cryst Solids 445–446:45–52. https://doi.org/10.1016/j.jnoncrysol.2016.05.006

18. Pharr GM, Oliver WC, Brotzen FR (1992) On the generality of the relationship among contact stiffness, contact area, and elastic modulus during indentation. J Mater Res 7:613–617

19. King RB (1987) Elastic analysis of some punch problems for a layered medium. Int J Solids Struct 23:1657–1664

20. Oliver WC, Pharr GM (1992) An improved technique for determining hardness and elastic modulus using load and displacement sensing indentation experiments. J Mater Res 7:1564–1583. https://doi.org/10.1557/jmr.1992.1564

21. Franco Jr. AR, Pintaúde G, Sinatora A, et al (2004) The use of a vickers indenter in depth sensing indentation for measuring elastic modulus and vickers hardness. Materials Research 7:483–491. https://doi.org/10.1590/s1516-14392004000300018

22. To T, Célarié F, Roux-Langlois C, et al (2018) Fracture toughness, fracture energy and slow crack growth of glass as investigated by the Single-Edge Precracked Beam (SEPB) and Chevron-Notched Beam (CNB) methods. Acta Mater 146:1–11. https://doi.org/10.1016/j.actamat.2017.11.056

23. Moore PB, Louisnathan SJ (1969) The crystal structure of fresnoite, Ba$_2$(TiO)Si$_2$O$_7$. Zeitschrift für Kristallographie 130:438–448

24. Uhlmann DR (1981) Crystal growth in glass-forming systems: a ten-year perspective. In: Simmons JH, Beall GH (eds) in Advances in Ceramics, Nucleation and Crystallization in Glasses. American Ceramic Society Inc, Columbus, pp 80–124

25. Santos R, Santos LF, Almeida RM, et al (2010) Crystallization of niobium germanosilicate glasses. J Solid State Chem 183:128–135. https://doi.org/10.1016/j.jssc.2009.10.031

26. James PF (1982) Nucleation in glass-forming Systems−A review. In: Simmons JH, Beau GH (eds) in Advances in Ceramics, Nucleation and crystallization of glasses. American Ceramic Society, Columbus, pp 14–48

27. Saha R, Nix WD (2002) Effects of the substrate on the determination of thin film mechanical properties by nanoindentation. Acta Mater 50:23–38. https://doi.org/10.1016/S1359-6454(01)00328-7

17

28. Rouxel T (2015) Driving force for indentation cracking in glass: composition, pressure and temperature dependence. Philosophical Transactions of the Royal Society A: Mathematical, Physical and Engineering Sciences 373:20140140

29. Joslin DL, Oliver WC (1990) A New Method for Analyzing Data from Continuous Depth-Sensing Microindentation Tests. J Mater Res 5:123–126. https://doi.org/10.1557/JMR.1990.0123

30. Mesarovic SDJ, Fleck NA (1999) Spherical indentation of elastic-plastic solids. Proceedings of the Royal Society A: Mathematical, Physical and Engineering Sciences 455:2707–2728. https://doi.org/10.1098/rspa.1999.0423

31. Sun K (1947) Fundamental condition of glass formation. Journal of the American Ceramic Society 30:277–281

32. Rouxel T (2017) Fracture surface energy and toughness of inorganic glasses. Scr Mater 137:109–113

18

Tables

Table 1. Glass code, composition, transition temperature (T_g), crystallization onset temperature (T_x), crystallization peak temperature (T_p), melting temperature (T_m), the ratio of glass transition-melting temperature (T_g/T_m), and thermal stability again crystallization ($T_x - T_g$) in BaO-TiO_2-SiO_2 glasses. The difference between nominal and actual compositions and experimental associated with the temperature measurement are better than ± 0.5 mol% and ± 5 °C, respectively.

Glass code	BaO (mol%)	TiO_2 (mol%)	SiO_2 (mol%)	T_g (°C)	T_x (°C)	T_p (°C)	T_m (°C)	T_g/T_m (-)	T_x-T_g (°C)
*x*00	30	0	70	705	821	860	1212	0.58	116
*x*05	30	5	65	727	868	914	1221	0.6	141
*x*10	30	10	60	736	876	932	1224	0.6	139
*x*15	30	15	55	751	889	931	1224	0.61	138
*x*20	30	20	50	759	877	907	1223	0.62	118
*x*25	30	25	45	761	842	855	1223	0.62	81
*x*30	30	30	40	762	830	841	1205	0.63	68

Table 2. Theoretical fracture surface energy of the possible crack paths.

Fracture possibility	Glass	Path 1	Path 2	Path 3
γ^t (J m^{-2})	1.68	0.81	1.44	1.98

19

Figures

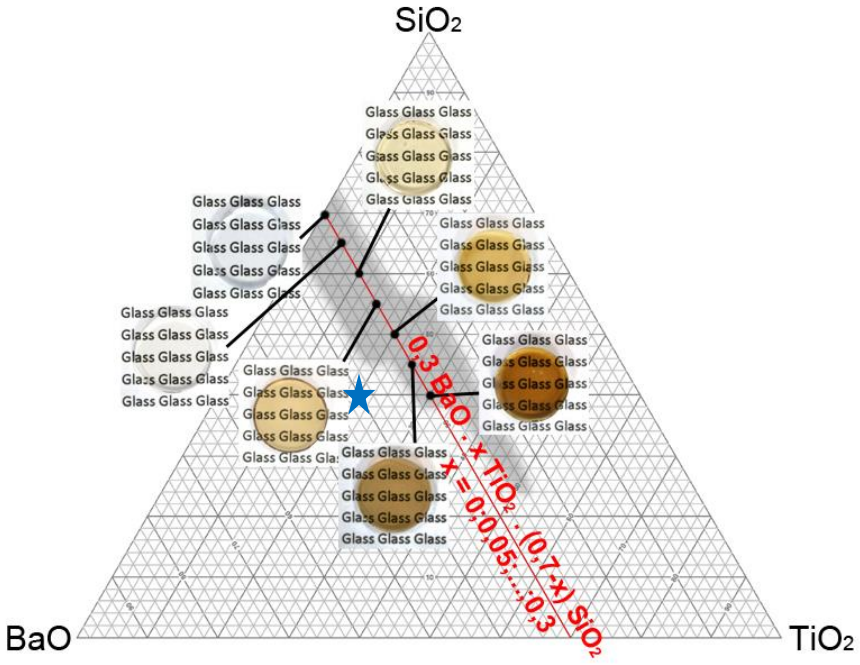

Figure 1. Composition diagram of the BaO-TiO_2-SiO_2 glass system. The black points indicate the studied glasses, i.e., 30BaO-*x*TiO_2-(70-*x*)SiO_2 where *x* varies from 0 to 30 mol%, and the blue star indicates the fresnoite composition (40BaO-20TiO_2-40SiO_2). The photo corresponding to the black point was taken from the glass sample with a diameter of 10 mm, thickness of 2 mm, and surfaces polished with 1 μm diamond paste. The grey zone represents the glass forming zone of the BaO-TiO_2-SiO_2 glass system after Ref. [16].

20

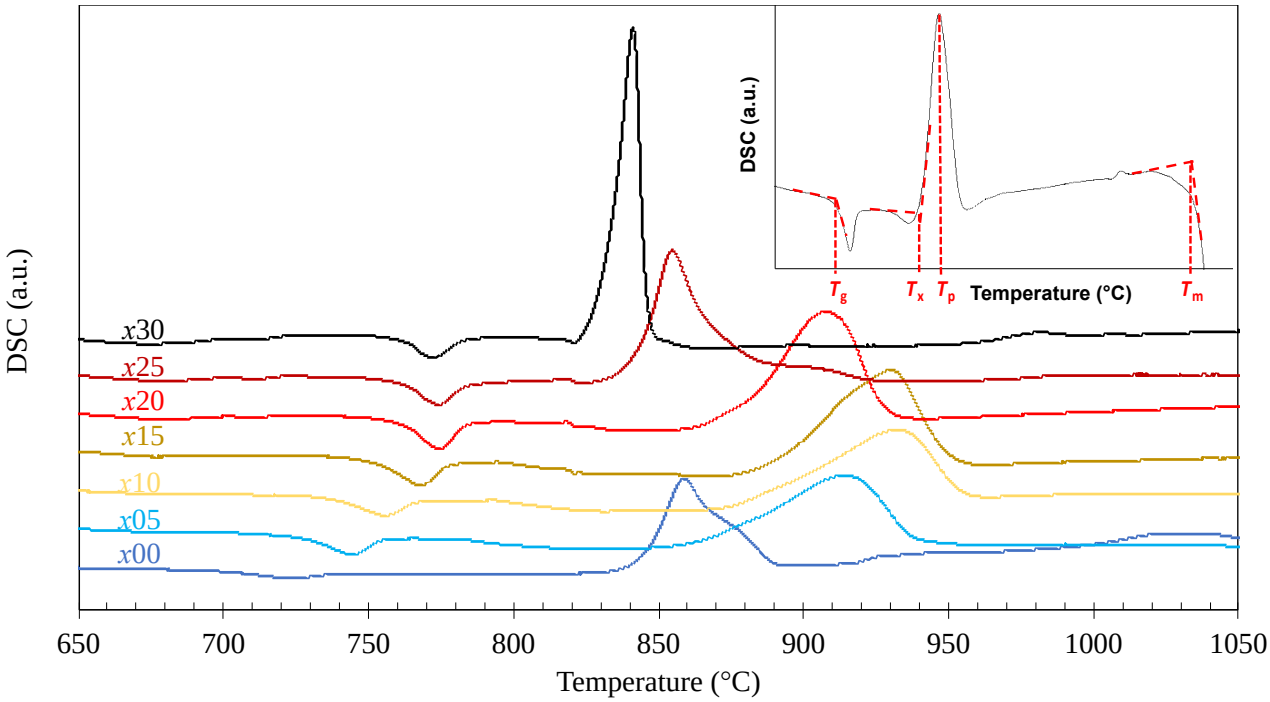

Figure 2. DSC curves for the $BaO\text{-}TiO_2\text{-}SiO_2$ glasses. The heating rate was 10 °C min^{-1}. The inset figure indicates the way the measurement of the different temperature parameters in Table 1 was done.

21

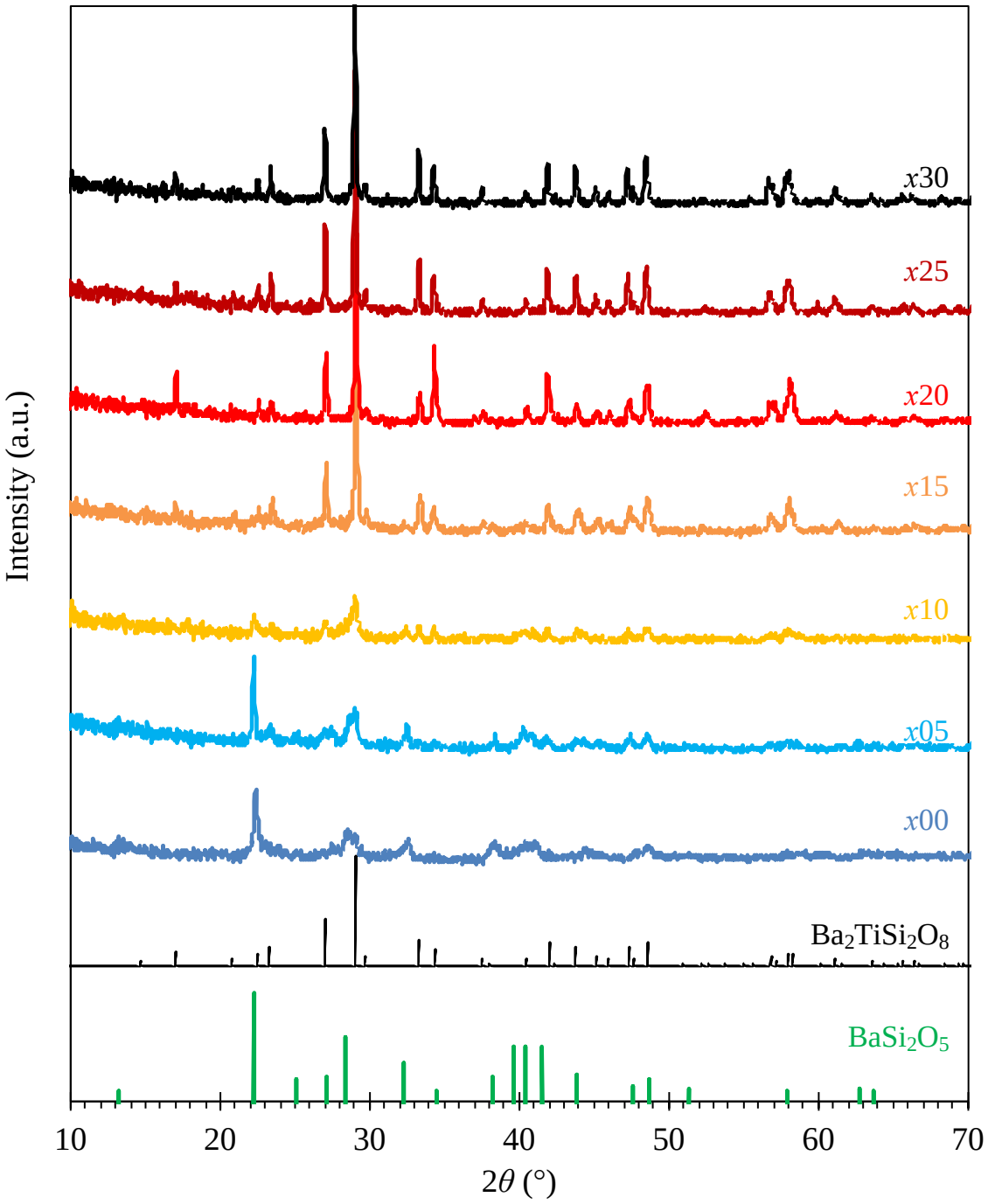

Figure 3. Powder XRD patterns for different glasses in this study, crystallized by heat-treatment at their T_p for 6 h, together with the $Ba_2TiSi_2O_8$ (ICDD: 00-022-0513) and $BaSi_2O_5$ (ICDD: 00-004-0382) crystals.

22

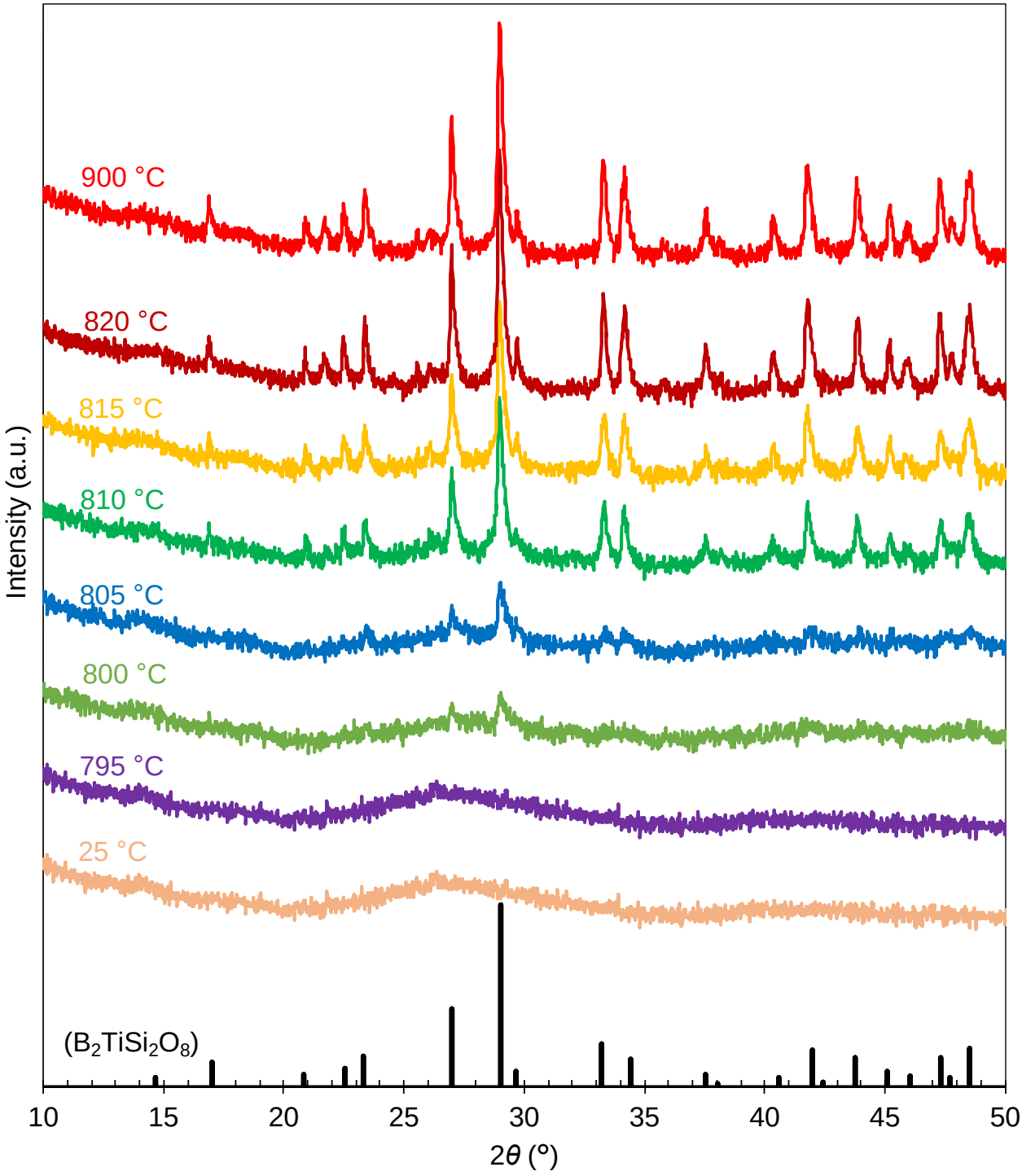

Figure 4. Powder XRD patterns for the *x*20 with temperatures at 25 °C, from 795 to 820 °C with 5 °C difference, and at 900 °C. These patterns are obtained from in-situ XRD experiments during heating from 25 °C to 900 °C, with a heating rate of 2 °C min^{-1}. The dark black lines correspond to the peaks of the $Ba_2TiSi_2O_8$ (ICDD: 00-022-0513).

23

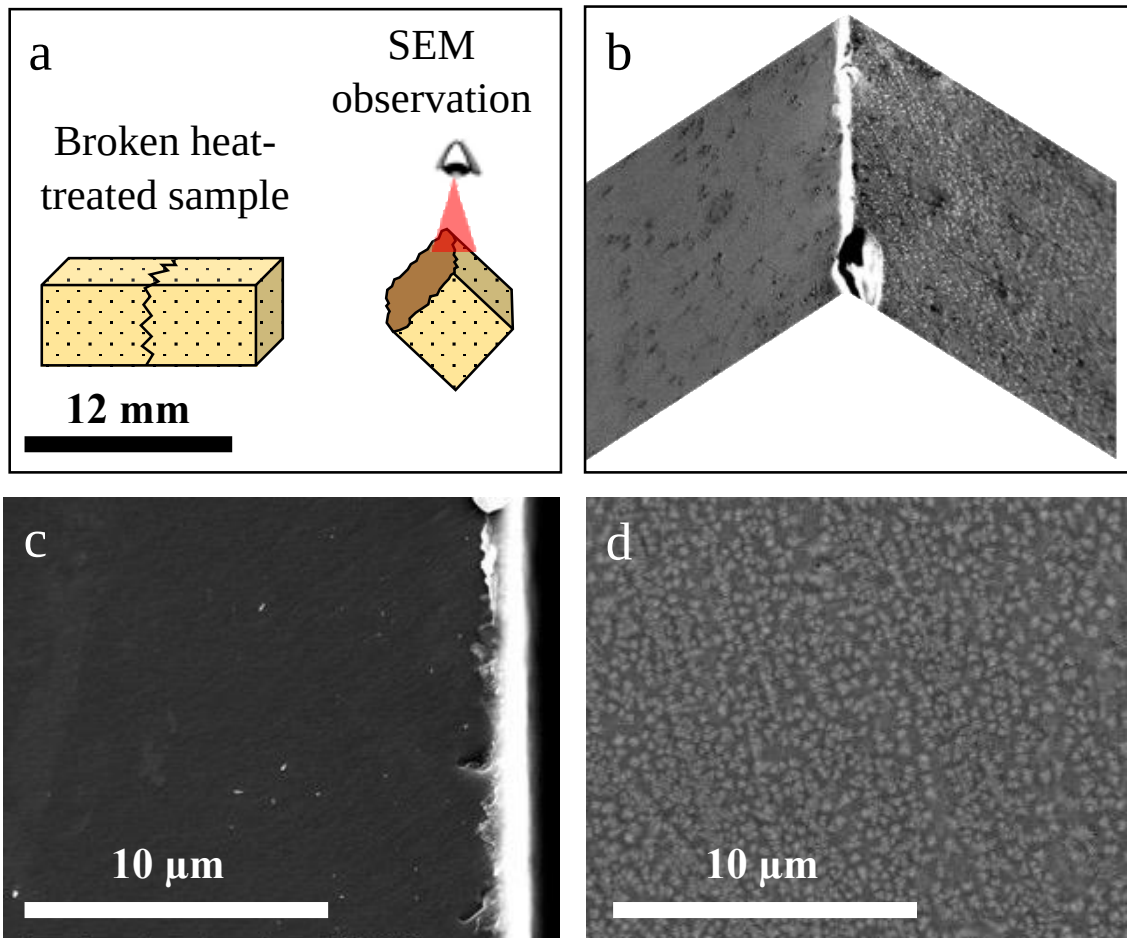

Figure 5. SEM observations for *x*20. (a). Breaking sample of *x*20 heat-treated at 800 °C for 2 h. (b). 3D view of the broken *x*20 beam. (c). Image on the broken surface of the heat-treated *x*20 (left-hand side of (b)). (d). image on the heat-treated surface (right-hand side of (b)) showing the average size of the crystals to be ~200 nm. The broken surface in Figure 5a is colored in brown.

24

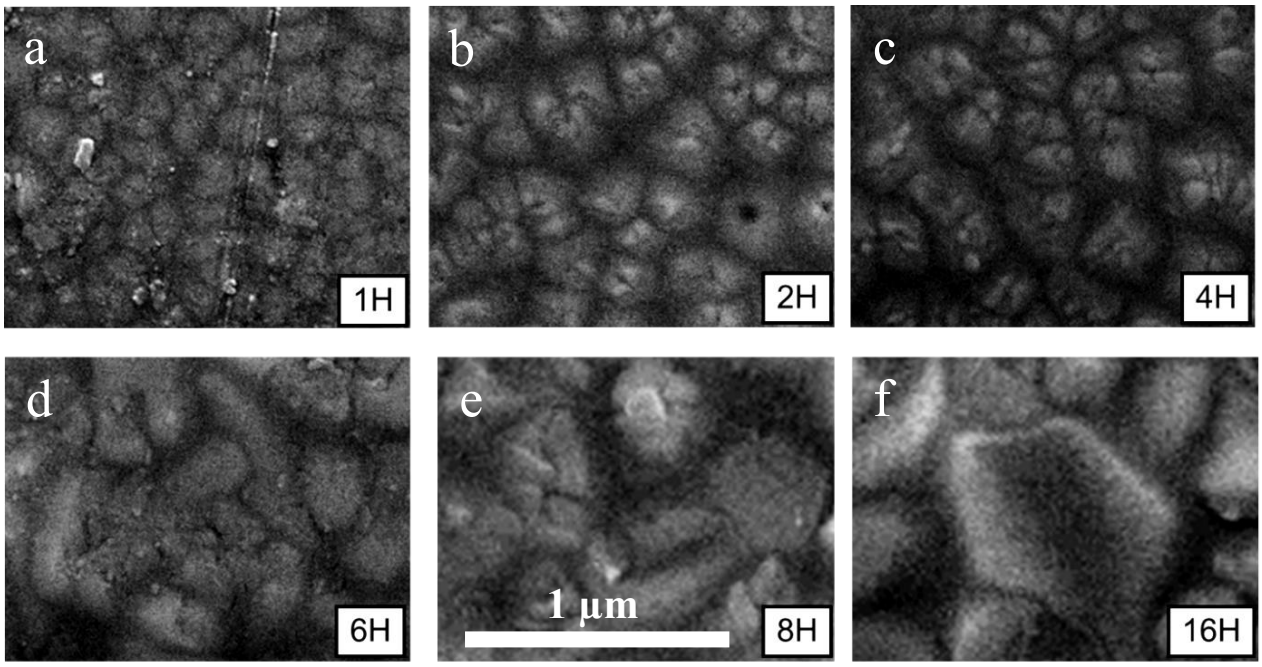

Figure 6. SEM images obtained from surface observation for crystallized glasses of *x*20 heat-treated at 800 °C for different duration times, i.e., 1 h (1H), 2 h (2H), 4 h (4H), 6 h (6H), 8h (8H), and 16 h (16H).

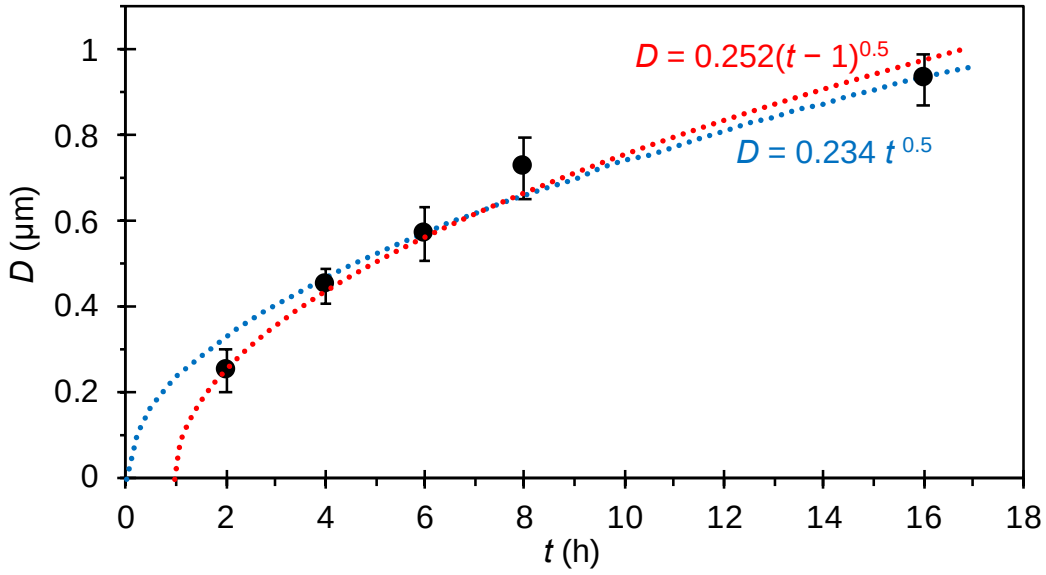

Figure 7. Evolution of average crystal diameter (*D*) with heat-treatment time (*t*). Each average crystal diameter was analyzed by the SEM images on at least, 50 crystals.

25

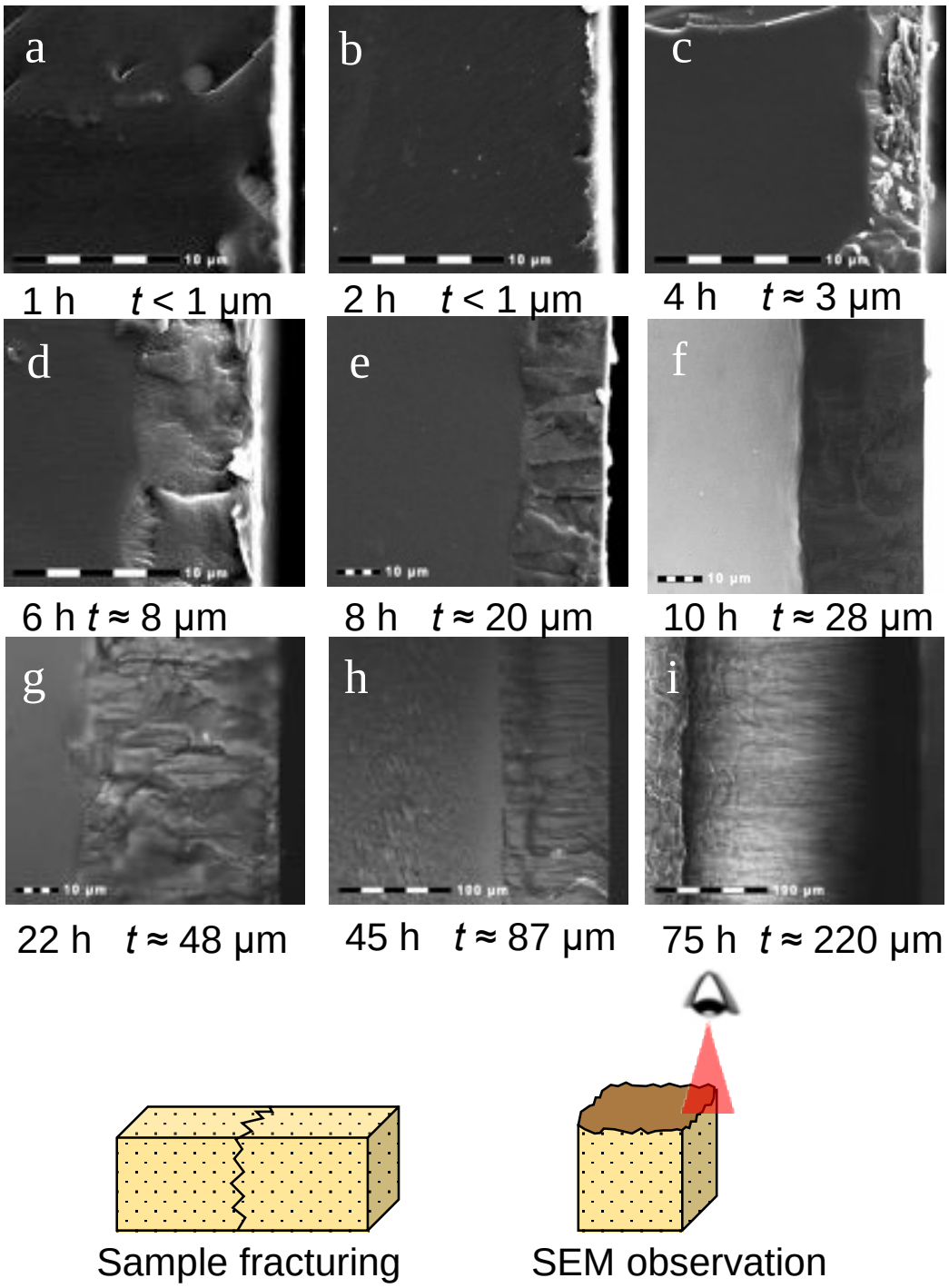

Figure 8. SEM images on the broken surface of the *x*20 after heat-treated at 800 °C for different duration times. (a). For 1 h and the depth (*P*) is < 1 µm. (b). For 2 h with *P* < 1 µm. (c). For 4 h with *P* ~ 3 µm. (d). For 6 h with *P* ~ 8 µm. (e). For 8 h with *P* ~ 20 µm. (f). For 10 h with P ~ 28 µm. (g). For 22 h with P ~48 µm. (h). For 45 h with P ~ 220 µm. (i). For 75 h with P ~ 220 µm. The schematic shows the observation technique in the SEM. The broken surface (observed surface) in schema below the SEM images is colored in brown.

26

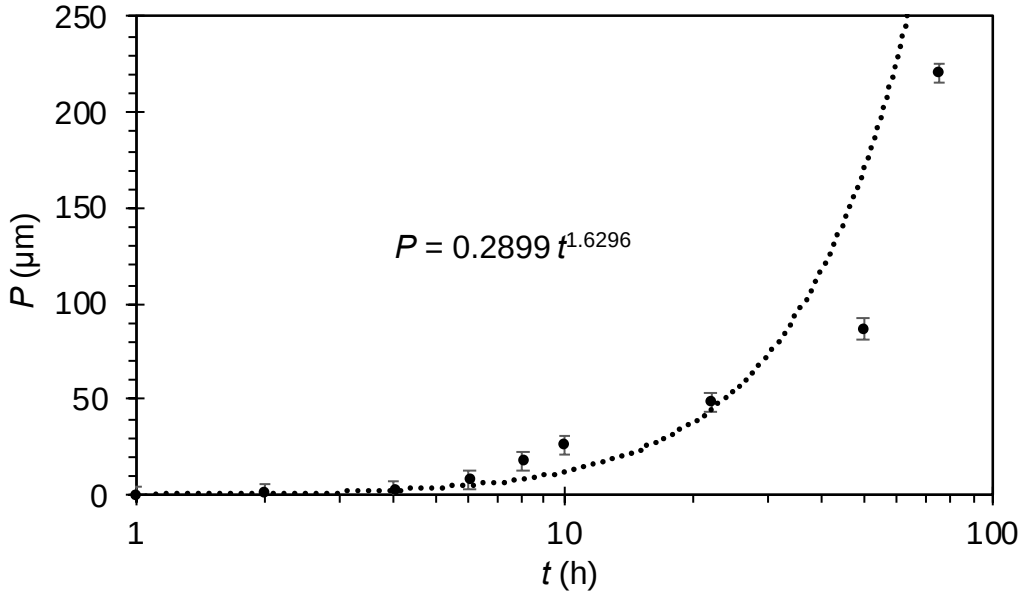

Figure 9. Evolution of crystalline depth (*P*) with heat-treatment duration (*t*). Each average crystal diameter was analyzed by the SEM images on at least, two samples (**Figure 8**).

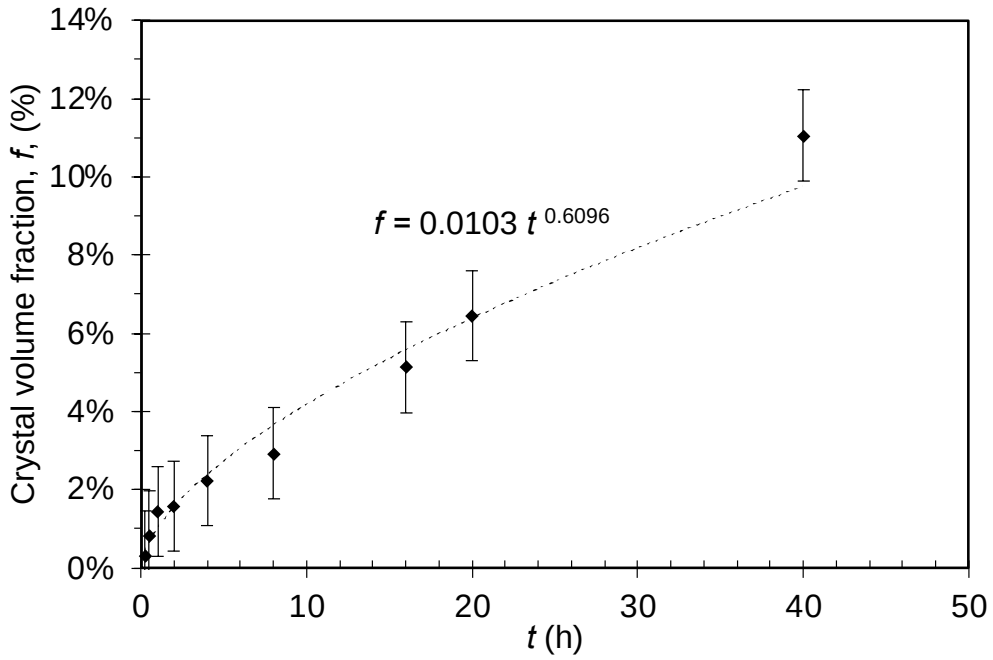

Figure 10. Crystal volume fraction (*f*) as a function of time (*t*). The dashed line is the power law regression. We note that this *f-t* curve represents only for the case study of mother glass sample with the thickness of 1 mm.

27

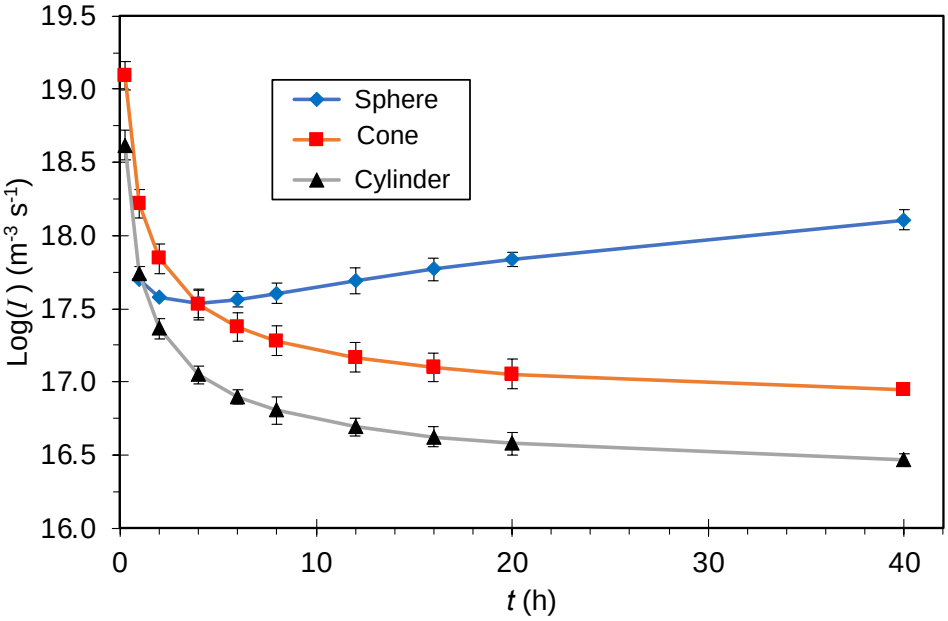

Figure 11. Nucleation rate (*I*) in logarithm as a function of heat-treatment time at 800 °C. *I* was calculated in three different shapes of crystals, i.e., sphere (blue), conic (red), and cylinder (black).

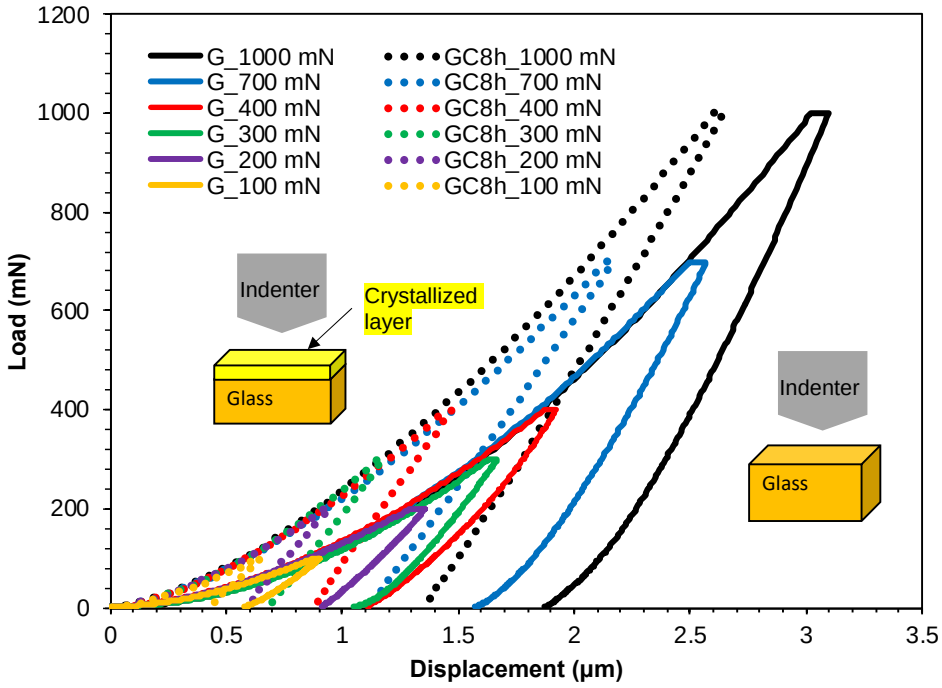

Figure 12. Load-displacement curves of *x*20 heat treated for 8 h at 800 °C (dotted line and noted as GC8h in legend) and *x*20 glass (solid line and noted as G). The indentation loads used in this study are 0.1 (gold), 0.2 (purple), 0.3 (green), 0.4 (red), 0.7 (blue), and 1 N (black). Grey, yellow and gold blocs represent the indentation tip, crystallized layer of *x*20 upon heat-treatment, and *x*20 glass, respectively.

28

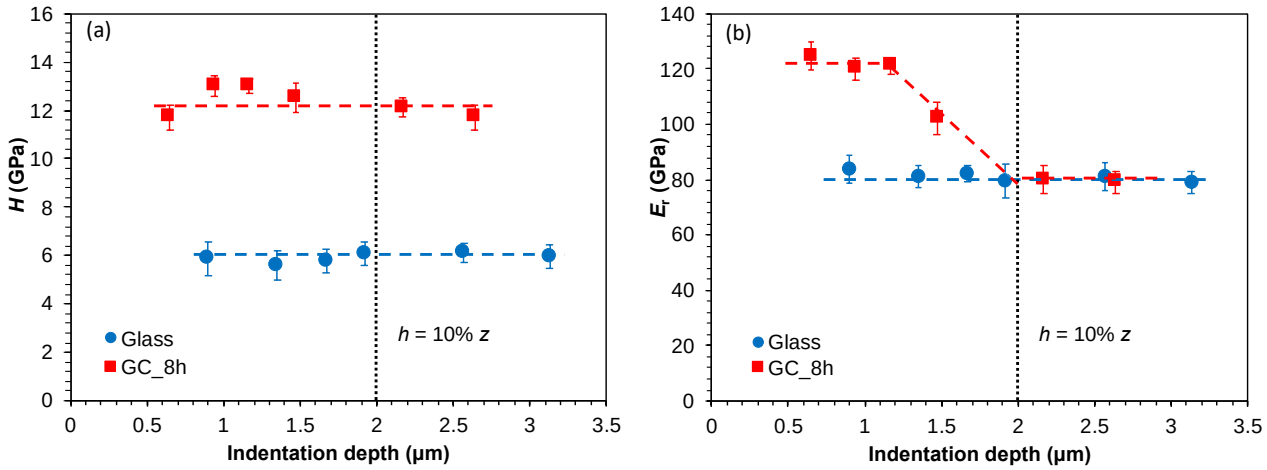

Figure 13. Hardness (H) and reduced modulus (E_r) of the glass and glass-ceramic (x20 heat treated at 8 h for 800 °C) as a function of indentation depth. The red and blue dashed lines are guided for the eyes. The black dotted line represents the indentation depth, which equals to 10 % of crystalline layer thickness, z.

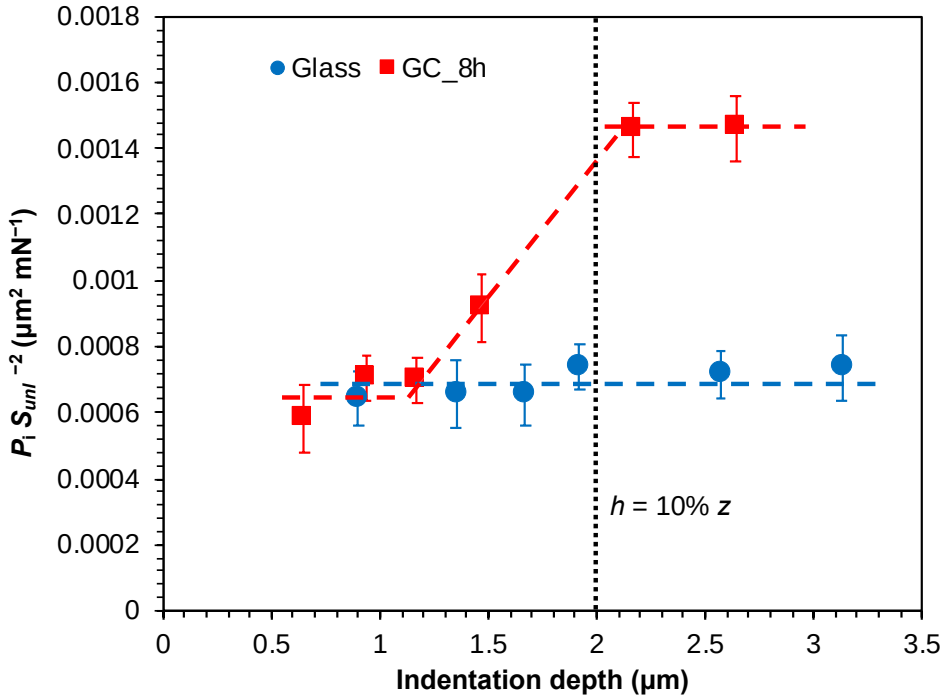

Figure 14. $P\ S_{unl}^{-2}$ vs. indentation depth of the x20 glass (square red point) and glass-ceramic (round blue point noted as GC_8h) with the crystalline thickness, z, of ~ 20 μm. The red and blue dashed lines are guided for the eyes. The black dotted line represents the indentation depth, which equals to 10 % of crystalline layer thickness.

29

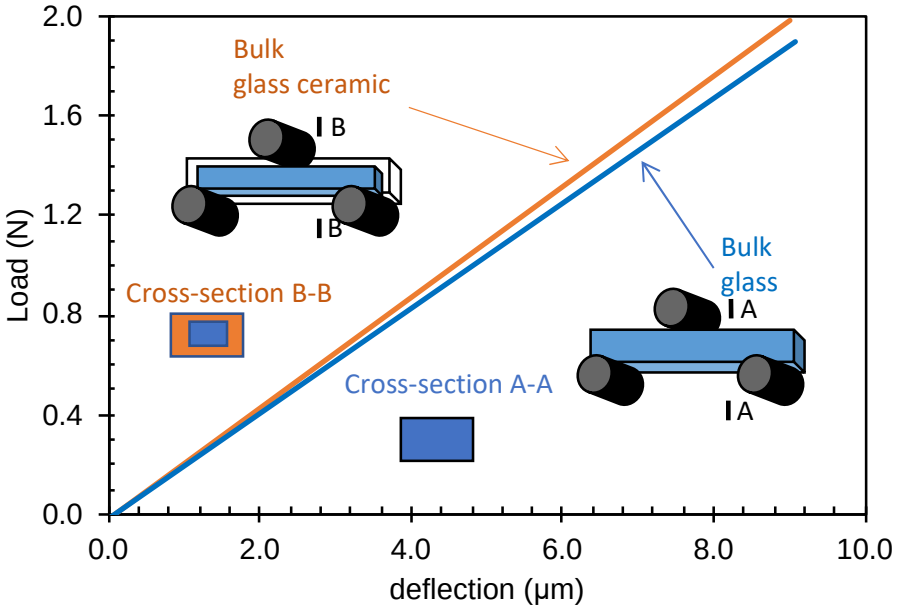

Figure 15. Load-deflection curves of three-point bending for *x*20 glass and glass-ceramic. The smooth line of the curves is obtained by averaging the data points of the three-point bending experiment. The curves with real data points are presented as Figure S4 in the Supporting Information.

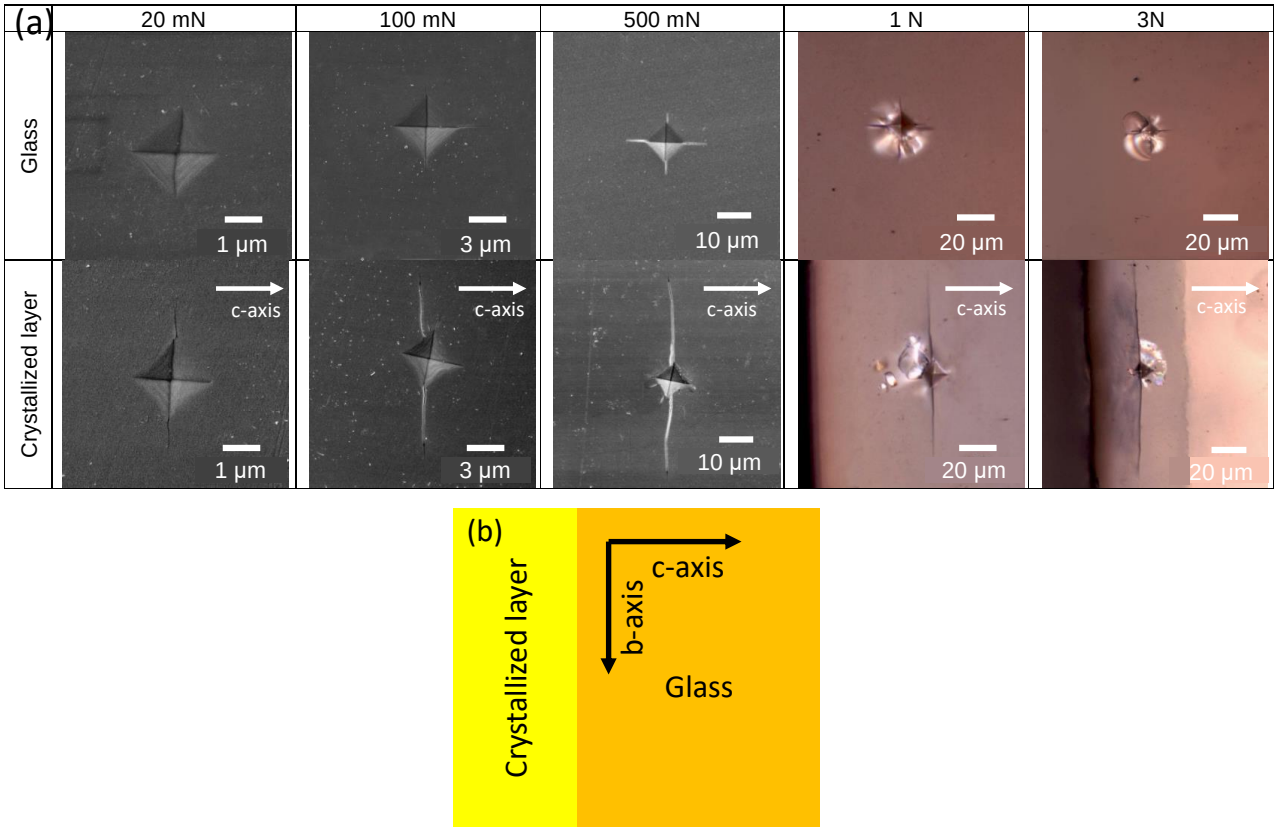

Figure 16. (a) Indentation observations by means of SEM for the loads of 0.02, 0.1, and 0.5 N, and optical microscope for the loads of 1 and 3 N for the *x*20 glass and glass-ceramic heat-treated for 75h at 800 °C. The white arrow shows the crystalline direction. (b) Schematic drawing of indented crystallized layer and glass matrix. The black arrows indicate the b- and the c-axis.

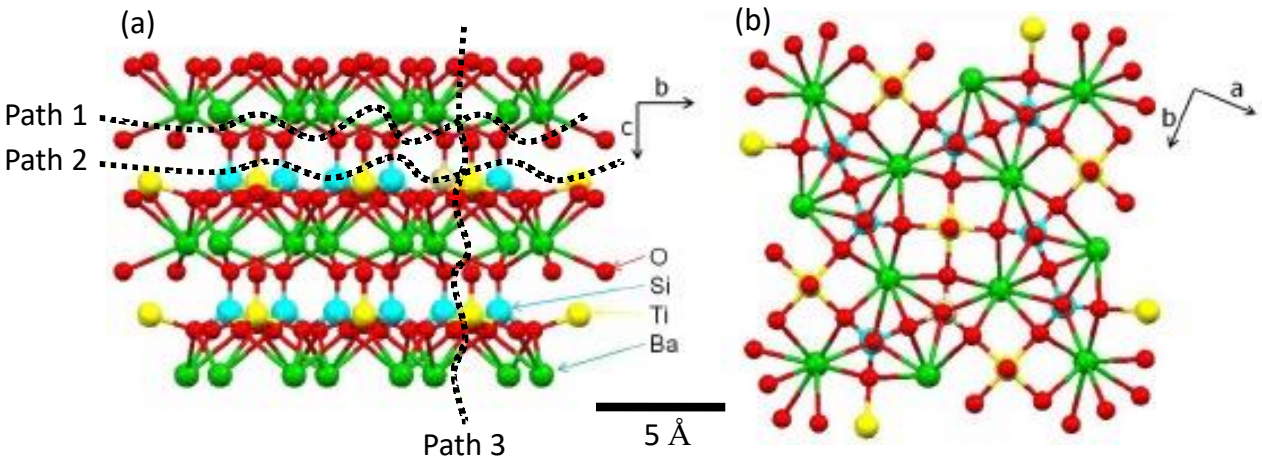

Figure 17. 3D visualization of the fresnoite structure obtained by the Mercury program based on the Inorganic Crystal Structure (4451-ICSD). (a) bc-plane. (b) ab-plane.

31